PHYSICAL REVIEW B VOLUME 53, NUMBER 15 15 APRIL 1996-I

Collective excitations of multishell carbon microstructures: Multishell fullerenes and coaxial nanotubes

Constantine Yannouleas, Eduard N. Bogachek, and Uzi Landman
School of Physics, Georgia Institute of Technology, Atlanta, Georgia 30332-0430

(Received 16 June 1995; revised manuscript received 27 November 1995)

σ and π plasmons in coaxial carbon nanotubes and multishell fullerenes are modeled in analogy with coupled collective excitations in finite, layered, two-dimensional-electron-gas, planar semiconductor superlattices. The curvature of the surface of these complex carbon clusters plays an important role in shaping the dimensionality (one dimensional, two dimensional, or three dimensional) of the plasmons. Direct crossover from a one-dimensional to a three-dimensional regime is found under readily fulfilled conditions for carbon nanotubes in the case of small finite longitudinal momentum transfer $\hbar q$, while for $q=0$ bulk graphitic plasmons fail to develop. For large q, a two-dimensional behavior is found. The case of multishell fullerenes resembles in all instances the $q=0$ behavior of carbon nanotubes. Such behavior correlates with the observed systematic redshift of the strong interstellar absorption band as compared to the π plasmon of bulk oriented graphite (i.e., the 5.7 eV position of the former compared to the 6.2 eV energy of the latter). Furthermore, in the case of π plasmons in carbon nanotubes, a special surface mode can develop for large q, due to the difference in the values of the dielectric constants between the graphitic structures and the surrounding medium.

I. INTRODUCTION

Collective electronic plasma excitations have been widely studied in a variety of physical systems characterized by various sizes and dimensionalities. Such excitations include bulk[1,2] and surface[3–6] plasmons in three-dimensional (3D) infinite and semi-infinite media, respectively; plasma excitations of two-dimensional (2D) electron gases (2DEG's), as in inversion layers in semiconductors[7] and at the surface of liquid helium;[8] coupled plasmons in planar *layered* 2DEG's, as in artificial semiconductor superlattices,[9–12] as well as in bulk graphite[13] (considered as a stack of planar graphitic sheets) and in graphite intercalation compounds;[14,15] and recently plasma excitations in nanometer-scale systems, as in atoms,[16,17] metal clusters,[18–20] and carbon clusters[21,22] (i.e., the C_{60} fullerene molecule[23]).

The present paper focuses on the coupled plasmons which can develop in carbon nanostructures made from graphene sheets curved to form superlattices of cylindrical or spherical symmetries, namely, coaxial carbon nanotubes[24,25] and concentric multishell fullerenes,[26,27] which are the latest carbon-based materials experimentally synthesized. Moreover, recent experimental work has observed plasma modes both in coaxial carbon nanotubes[28–30] [i.e., σ and π excitations by means of parallel electron energy loss spectroscopy (PEELS)] and in multishell fullerenes[31] (i.e., π excitations by means of ultraviolet absorption). It has also been suggested[31–34] that the well known strong interstellar absorption band[35,36] centered at 217.5 nm (5.7 eV) is related to multishell fullerenes.

The present work will show that the ability to prepare such carbon structures with variable numbers of coaxial sheets (or concentric shells) offers unique opportunities for exploration of the effects of dimensionality on the nature of collective excitations in *curved* low-dimensional electron-gas superlattices. In particular, we will show that a succession of dimensionality crossovers [e.g., from one-dimensional (1D) to 3D, and then to 2D] may occur in carbon nanotubes as a function of the number of graphitic sheets N and of the longitudinal plasmon wavelength q, and that such crossovers may account for the main experimentally observed trends.[28–30] In contrast, multishell fullerenes, lacking the infinite longitudinal direction, fail to develop a bulk (3D) plasmon. Rather, their behavior is similar to that of coaxial carbon nanotubes in the limit of $q=0$. Such behavior is of particular interest, since it may underlie the systematic redshift of the interstellar absorption band, believed to be associated with multishell fullerenes, as compared to the π plasmon in coaxial carbon nanotubes[28] and in the bulk oriented graphite[37] (the redshift amounts to 0.5 eV if the bulk plasmon is taken at 6.2 eV according to Refs. 32 and 37).

Moreover, in the case of π plasmons, we show that it is essential to account for the difference in the dielectric constants between the carbon structures (ϵ) and the surrounding medium (ϵ_m). In the case of carbon nanotubes, we predict that for large q this difference will result in a special surface plasmon, in analogy with the surface plasmons of semiconductor supperlattices[11,12] and of semi-infinite graphite intercalation compounds.[15]

Some earlier investigations by us of σ plasmons in coaxial carbon nanotubes, using a semiclassical random-phase approximation (RPA) formulation (with the simplification that $\epsilon=\epsilon_m=1$), have been briefly discussed in Ref. 38. The dispersion of coupled plasmons as a function of q in coaxial carbon nanotubes with $N\leqslant 4$ sheets has also been studied earlier.[39,40] As we discussed previously,[38] such a small number of tubules precludes the development of the bulk graphitic plasmon. Concerning dimensionality crossovers, such a small assembly exhibits strong similarities with the case of a single tubule, where only a 1D to 2D crossover can develop[41] [see also Fig. 2(b) in Ref. 38].

We further mention here another investigation,[42] which used a hydrodynamical approach in conjunction with a model of multishell fullerenes consisting of concentric shells of *finite* width. Rich spectra of collective excitations were found for multishell fullerenes with $N \leqslant 40$ shells, but the associated matrix equations were rather complex (due to the finite width of the shells), and thus inhibited any investigations concerning the development of the bulk graphitic plasmon and of the emergence, or not, of dimensionality crossovers.

Finally, we mention that Refs. 39, 40, and 42 have restricted their investigations to the simplest case $\epsilon = \epsilon_m = 1$. Using a different approach, Lucas *et al.*[32] have developed a model for multishell fullerenes with $\epsilon \neq \epsilon_m$ by assuming full transferability (or conformal invariance, see Ref. 28) of the dielectric tensor of bulk (3D) planar graphite to the spatial dimensions and curved geometry of multishell carbon microstructures. However, the richness of dimensionality regimes (1D and 2D in addition to 3D) revealed by our studies suggests that such transferability of the bulk planar-graphite dielectric tensor to the nanometer-scale multishell fullerenes is questionable.

II. THEORY OF COUPLED PLASMONS IN CURVED FINITE SUPERLATTICES

Plasmon modes are commonly described in the random-phase approximation method of the linear response theory.[1] At the microscopic, atomistic and molecular, level, this method[43] allows one to incorporate the particular atomic or molecular structure of the ground state of the system, and has been successfully applied to a variety of microsystems, such as atoms,[16,17] metallic clusters,[20] and the C_{60} molecule.[22] However, the more complicated the electronic structure of the ground state, the more computationally demanding the associated RPA equations become. For multiunit structures like coaxial carbon nanotubes and multishell fullerenes, for which the precise electronic structure of the ground state is unknown, the computational treatment of the RPA equations describing the coupled plasmons is rather prohibitive. Consequently, we have adopted a simple variant of the hydrodynamical method, which has been used in the field of planar layered semiconductor superlattices.[9–12] Accordingly, we view each shell as a two-component *curved* 2DEG exhibiting σ- and π electron plasma modes. Since it neglects quantal size effects [e.g., the influence of individual particle-hole excitations (Landau damping) or the effects of electronic spill-out, see e.g., Ref. 20], this approach does not provide a complete description for each graphene sheet (or shell), but nonetheless it becomes advantageous for the case of many sheets (or shells), since it captures the essential features of the coupling between sheets (or shells) due to the Coulomb field.[38]

We model coaxial carbon nanotubes and multishell fullerenes as two-dimensional cylindrical and spherical electron-gas layers coupled through their mutual electric fields. In such superlattices, undamped plasma excitations can be described by Newton's equation of motion for the electrons, in conjunction with the continuity and Poisson equations. In the linear approximation, one has

$$m_e \frac{\partial \mathbf{v}^i}{\partial t} = e \nabla \Phi(r = R_i), \tag{1}$$

$$\frac{\partial n_1^i}{\partial t} + n_0^i \nabla \mathbf{v}^i = 0, \tag{2}$$

$$\Delta \Phi(\mathbf{r}) = 0, \quad r \neq R_i, \tag{3}$$

where m_e is the electronic mass, and $\mathbf{v}^i$ is the velocity of the electrons residing on the ith shell whose radius is R_i. n_0^i and n_1^i are the values of the equilibrium electronic density (associated with the ith shell) and its small perturbation due to the plasma oscillation, respectively. Finally, $\Phi(\mathbf{r})$ is the total electrostatic potential. We note that the equations of motion and continuity [Eqs. (1) and (2)] are restricted to the surface of each shell, and thus the velocity vector $\mathbf{v}^i$ is two-dimensional in character, and $-\nabla\Phi$ represents the tangential component of the electric field. We further note that the Laplacian in the Poisson equation (3) is naturally of a three-dimensional character.

To solve the system of Eqs. (1)–(3), we have to provide appropriate boundary conditions. We denote as Φ_i the potential in the region $R_{i-1} \leqslant r \leqslant R_i$ between two successive shells $i-1$ and i with $i = 2, \ldots, N$. In the innermost region $r \leqslant R_1$, we denote the potential as Φ_1, while in the outermost region $R_N \leqslant r$, the potential is denoted as Φ_{N+1}. These boundary conditions are given by

$$\Phi_i(R_i) = \Phi_{i+1}(R_i), \tag{4}$$

and by

$$\frac{\partial \Phi_{i+1}(R_i)}{\partial r} - \frac{\partial \Phi_i(R_i)}{\partial r} = 4\pi e n_1^i. \tag{5}$$

In writing Eq. (5), we assumed that the dielectric constant of the carbon microstructures (ϵ) is equal to the dielectric constant of the surrounding medium (ϵ_m), which is further assumed to be air or vacuum, i.e., $\epsilon = \epsilon_m = 1$. As will be elaborated later (Sec. III B 3), the assumption that $\epsilon = \epsilon_m = 1$ is a valid approximation for the case of σ plasmons (for the case of π plasmons,[44] see below; the generalized matrix equations for $\epsilon \neq \epsilon_m$ are given in the Appendix).

Assuming a harmonic dependence for all quantities as a function of time [$\sim \exp(-i\omega t)$, where ω is the frequency of a coupled plasmon], we obtain from Eqs. (1) and (2) after the elimination of the velocity $\mathbf{v}^i$

$$m_e \omega^2 n_1^i = n_0^i e \Delta \Phi(r = R_i). \tag{6}$$

Combining Eqs. (3) and (6), and the boundary conditions (4) and (5), one can derive a secular eigenvalue equation for the coupled-plasmon frequencies in the form

$$m_e \omega^2 n_1^i = \sum_{j=1}^{N} M_{ij} n_1^j, \tag{7}$$

where the indices i and j denote different shells of the multishell structure. Specific expressions for the matrix M in the cases of coaxial carbon nanotubes and of multishell fullerenes will be derived in the next two subsections.

A. Eigenvalue equation for coaxial carbon nanotubes

Due to the cylindrical symmetry of carbon nanotubes, one can replace the quantities n_1^i and Φ in Eqs. (3) and (6) by expressions of the form

$$n_1^i(\phi,z)=\tilde{n}_1^i\exp(im\phi)\exp(iqz), \tag{8}$$

and

$$\Phi(r,\phi,z)=\tilde{\Phi}(r)\exp(im\phi)\exp(iqz), \tag{9}$$

where m is the integer azimuthal quantum number, and q is the longitudinal wave vector. After substitution, one finds

$$m_e\omega^2\tilde{n}_1^i=-n_0^i e\left(\frac{m^2}{R_i^2}+q^2\right)\tilde{\Phi}_i(R_i), \tag{10}$$

and

$$\frac{\partial^2\tilde{\Phi}}{\partial r^2}+\frac{1}{r}\frac{\partial\tilde{\Phi}}{\partial r}-\left(\frac{m^2}{r^2}+q^2\right)\tilde{\Phi}=0, \quad r\neq R_i. \tag{11}$$

The solution of Eq. (11) has the general form

$$\tilde{\Phi}_1=A_1I_m(qr),$$

$$\tilde{\Phi}_i=A_iI_m(qr)+B_iK_m(qr), \quad i=2,3,\ldots,N,$$

$$\tilde{\Phi}_{N+1}=B_{N+1}K_m(qr), \tag{12}$$

where $I_m(x)$ and $K_m(x)$ are modified Bessel functions.[45]

The coefficients A_i and B_i in Eq. (12) can be expressed as functions of the perturbation densities $\tilde{n}_1^i$ by using the boundary conditions (4) and (5). A subsequent substitution[46] for $\tilde{\Phi}_i$ in Eq. (10) yields the matrix eigenvalue quation,

$$\omega^2\tilde{n}_1^i=\sum_{j=1}^{N} M_{ij}^{\text{tub}}\tilde{n}_1^j, \tag{13a}$$

where the matrix elements M_{ij}^{tub} are given by the expression

$$M_{ij}^{\text{tub}}=\frac{4\pi n_0^i e^2}{m_e}R_j\left(\frac{m^2}{R_i^2}+q^2\right)I_m(qR_<)K_m(qR_>). \tag{13b}$$

In Eq. (13b), $R_<\equiv\min(R_i,R_j)$ and $R_>\equiv\max(R_i,R_j)$.

In the case of a single tubule (i.e., $N=1$) with label i, it follows from Eq. (13) that the plasmon frequency is given as[40]

$$\omega_{0i}^2=\frac{4\pi n_0^i e^2}{m_e}R_i\left(\frac{m^2}{R_i^2}+q^2\right)I_m(qR_i)K_m(qR_i). \tag{14}$$

From Eq. (14), two different dimensionality regimes can be distinguished[40,41] depending on the limiting cases $qR_i\gg|m|$ and $qR_i\ll|m|$. For this we use the well known limiting forms of the modified Bessel functions,[45] namely,

$$x\ll1, \quad I_m(x)\rightarrow\frac{1}{\Gamma(m+1)}\left(\frac{x}{2}\right)^m,$$

$$K_m(x)\rightarrow\begin{cases}-\left[\ln\left(\dfrac{x}{2}\right)+0.5772\ldots\right], & m=0\\[2ex] \dfrac{\Gamma(m)}{2}\left(\dfrac{2}{x}\right)^m, & m\neq0;\end{cases} \tag{15}$$

$$x\gg1,m, \quad I_m(x)\rightarrow\frac{1}{\sqrt{2\pi x}}e^x\left[1+0\left(\frac{1}{x}\right)\right],$$

$$K_m(x)\rightarrow\sqrt{\frac{\pi}{2x}}e^{-x}\left[1+0\left(\frac{1}{x}\right)\right]. \tag{16}$$

As a result of the limits displayed in Eq. (16), Eq. (14) in the limit $qR_i\gg|m|$ yields

$$\omega_{0i}^2\approx\frac{2\pi n_0^i e^2}{m_e}q, \tag{17}$$

which corresponds to a proper 2D behavior[47] (namely, the plasmon energy is proportional to the square root of q), since the longitudinal momentum transfer $\hbar q$ is a continuous variable.

In the opposite limit $qR_i\ll|m|$, Eq. (14) yields with the help of Eq. (15) for $m\neq0$

$$\omega_{0i}^2\approx\frac{2\pi n_0^i e^2}{m_e}\frac{m}{R_i}, \quad m\neq0, \tag{18}$$

which may be viewed as 2D in character when $m/R_i\gg1$, since m/R_i is then a *quasicontinuous* effective wave vector along the perimeter of the cylinder. However, for small values of the discrete azimuthal quantum number m, the right-hand side (RHS) of Eq. (18) depends strongly on the radius of the tube, unlike the case of Eq. (17) where the plasmon frequency is independent of the dimensions of the tube. This latter case cannot be properly characterized as 2D, and we will adopt the convention of referring to it as a 1D case.

For $m=0$ and $qR_i\ll1$, the plasmon excitation has a traditional one-dimensional character,[48,49] namely, it exhibits (up to a slowly varying factor of the square root of a logarithmic term) a linear dependence on q,

$$\omega_{0i}^2\approx\frac{4\pi n_0^i e^2R_i}{m_e}q^2\ln(1.123/qR_i), \quad m=0. \tag{19}$$

In the case of two coaxial tubes, naturally, there are two modes with frequencies given by the expression

$$\omega_{1,2}^2=\frac{1}{2}(\omega_{01}^2+\omega_{02}^2)\pm\sqrt{\frac{1}{4}(\omega_{01}^2-\omega_{02}^2)^2+F_{12}\omega_{01}^2\omega_{02}^2}, \tag{20}$$

where

$$F_{12}=\frac{I_m(qR_1)K_m(qR_2)}{I_m(qR_2)K_m(qR_1)}. \tag{21}$$

When $q(R_2-R_1)\gg1$, the tubules decouple (i.e., $F_{12}\approx0$) and oscillate independently of each other with frequencies $\omega_{1,2}\approx\omega_{01},\omega_{02}$ [see Eq. (14)].

In the special case when the longitudinal wave vector is zero ($q=0$), the matrix elements M_{ij}^{tub} for the case of N tubules reduce to the expression

$$M_{ij}^{\text{tub}}(q=0)=\frac{2\pi n_0^i e^2}{m_e} m \frac{R_j}{R_i^2}\left(\frac{R_<}{R_>}\right)^m, \quad m\neq 0. \tag{22}$$

As we will see below, this special case of the cylindrical symmetry has strong similarities to the spherical case associated with multishell fullerenes.

B. Eigenvalue equation for multishell fullerenes

Multishell fullerenes are modeled as concentric spherical shells, in which case the density perturbations n_1^i on each shell and the electrostatic potential are of the form

$$n_1^i(\theta,\phi)=\tilde{n}_1^i Y_{lm}(\theta,\phi), \tag{23}$$

$$\Phi(r,\theta,\phi)=\tilde{\Phi}(r)Y_{lm}(\theta,\phi), \tag{24}$$

where Y_{lm} denote the spherical harmonics.

Using Eqs. (23) and (24), we obtain from Eqs. (6) and (3)

$$m_e\omega^2\tilde{n}_1^i=-n_0^i el(l+1)\frac{1}{R_i^2}\tilde{\Phi}(R_i), \tag{25}$$

$$\frac{\partial^2\tilde{\Phi}}{\partial r^2}+\frac{2}{r}\frac{\partial\tilde{\Phi}}{\partial r}-\frac{l(l+1)}{r^2}\tilde{\Phi}=0, \quad r\neq R_i. \tag{26}$$

The solutions of Eq. (26) have the general form

$$\tilde{\Phi}_1(r)=A_1 r^l,$$

$$\tilde{\Phi}_i(r)=A_i r^l+B_i r^{-l-1}, \quad i=2,3,\ldots,N,$$

$$\tilde{\Phi}_{N+1}(r)=B_{N+1}r^{-l-1}. \tag{27}$$

The coefficients A_i and B_i in Eq. (27) can be expressed as functions of the densities $\tilde{n}_1^i$ by using the boundary conditions (4) and (5). A subsequent substitution[46] for $\tilde{\Phi}$ in Eq. (25) yields the matrix equation

$$\omega^2\tilde{n}_1^i=\sum_{j=1}^{N} M_{ij}^{\text{fuller}}\tilde{n}_1^j, \tag{28a}$$

where the matrix elements are given by

$$M_{ij}^{\text{fuller}}=\omega_{0i}^2\begin{cases}(R_i/R_j)^{l-1}, & i\leqslant j\\ (R_j/R_i)^{l+2}, & i>j,\end{cases} \tag{28b}$$

with ω_{0i} the frequency of a single shell (ith shell) given by[50]

$$\omega_{0i}^2=\frac{4\pi n_0^i e^2}{m_e}\frac{l(l+1)}{2l+1}\frac{1}{R_i}. \tag{28c}$$

It is seen that the matrix in Eq. (28) has a strong similarity with the matrix in Eq. (22) valid for coaxial nanotubes in the limiting case of $q=0$.

We note that expression (28c) for the plasmon frequency of a single shell depends on the sphere radius R_i and that it becomes smaller the larger the radius, approaching a vanishing value for $R_i\rightarrow\infty$. In this respect, the plasmons of single-shell hollow fullerenes contrast with the surface plasmons of metal clusters,[20] whose energy for large radii approaches the classical Mie constant[51,52] associated with a solid metallic sphere.

We further notice that for $l\gg 1$ and $l/R_i\gg 1$ (quasicontinuum case) the plasmon frequencies (28c) have a two-dimensional character with respect to the effective wave vector l/R_i, namely,

$$\omega_{0i}^2\rightarrow\frac{2\pi n_0^i e^2}{m_e}\frac{l}{R_i}. \tag{29}$$

In the case of only two spherical shells, the plasma frequencies are given by the same expression as Eq. (20), but the constant F_{12} is now given by

$$F_{12}^{\text{fuller}}=(R_1/R_2)^{2l+1}. \tag{30}$$

In the limit $R_1\ll R_2$, or $l\gg 1$, the two shells decouple and oscillate independently of each other with frequencies given by Eq. (28c).

In the following sections, we will present an analysis of coupled plasmons in coaxial carbon nanotubes and multishell fullerenes with $N>2$ based on numerical solutions of the eigenvalue equations (13) and (28).

III. NUMERICAL INVESTIGATIONS

A. Qualitative considerations and interpretative framework

One of the aims of our investigation is to inquire whether the matrix eigenvalue equation (7), specified for the cases of coaxial carbon nanotubes and multishell fullerenes, can yield among its multitude of solutions a volume plasmon identical to the 3D plasmon of bulk graphite. For qualitative considerations in this subsection, it will be sufficient to restrict the presentation to the case of unscreened σ plasmons with $\epsilon=\epsilon_m=1$ (for screened σ plasmons[44] with $\epsilon=0.8$ and $\epsilon_m=1$, see the last paragraph of Sec. III B 3). The dispersion relation of the plasmon of bulk graphite is given by the expression

$$\omega(q)=\omega_p^{\text{bulk}}+cq^2, \tag{31}$$

where the long-wavelength plasmon energy $\hbar\omega_p^{\text{bulk}}$ is a constant,

$$\omega_p^{\text{bulk}}=[4\pi e^2 n/(m_e d)]^{1/2}, \tag{32}$$

and the proportionality coefficient[10] $c=(3/16)v_F^2/\omega_p^{\text{bulk}}$, v_F being the Fermi velocity of the 2DEG on each graphitic sheet.

In Eq. (32), n is the areal electronic density on a planar graphitic sheet (we take n to be equal to $0.319a_0^{-2}$ for the density of σ electrons), and d is the interlayer distance of planar graphite ($d=6.4a_0$). The ratio n/d defines an effective volume density, and therefore Eq. (32) represents the corresponding volume (3D) plasmon.[9,10] Using the above parameters for the densities n and interlayer distance d, one finds that the bulk graphite, unscreened σ plasmon energy in our model is 21.53 eV (the mass m_e is taken equal to the free electron mass).

The plasmon energies in the cases of a single tubule (or spherical shell) and of a pair of coupled tubules (or spherical shells) were given in Sec. II. We note that these energies depend explicitly on the inner- and outermost radii of the assembly, unlike the bulk plasmon [see Eq. (32)], which must be independent of the geometric parameters of the curved superlattices (with the exception naturally of the interlayer distance). We further note that, when we calculate in the next section the case of nanotubes or multishell fullerenes with an arbitrary number N of shells, the areal densities on each tube (or shell) and the intertubule (or intershell) distance will be kept equal to the corresponding quantities of planar graphitic sheets in agreement with experimental evidence from carbon nanostructures.[24,27]

We first address the case of coaxial carbon nanotubes. In investigating whether a 3D plasmon can emerge in coaxial carbon nanotubes, we will study the behavior of the solutions of Eq. (13) in the following two ways.

(1) Starting with a single tubule, and keeping the longitudinal wave vector q constant, we will successively consider additional tubules in order to study the evolution of the coupled plasmon mode with a given azimuthal angular momentum m as a function of the number N of tubules.

(2) Keeping the number N of tubules in the assembly constant, we will investigate the evolution of the coupled-plasmon mode for a given m as a function of the longitudinal wave vector q.

In the case of multishell fullerenes, the two possibilities described above are reduced to the first one, since, in place of the pair of quantum numbers m and q, the spherical symmetry allows the angular momentum l to solely control the plasmon energy. Furthermore, from the similarities in the general form of the matrix elements M_{ij} between the spherical symmetry and the cylindrical one in the limiting case when the longitudinal wave vector is zero, namely, $q=0$, we can surmise that the spherical case is closely related to this special subcase of the cylindrical symmetry. Anticipating our results (see below), we mention here that a nonzero value of q is essential for the emergence of the bulk plasmon in coaxial carbon nanotubes, and that such a bulk plasmon cannot be developed in multishell fullerenes.

Before proceeding to describe actual numerical investigations of the matrix equations (13) and (28) for curved geometries, it is useful to refer to earlier results obtained in connection with planar semiconductor superlattices.[9,12] In the case of a finite planar lattice, an eigenvalue problem like Eq. (7) yields a set of N modes organized in a band,[12] the plasmon mode being the uppermost one whose energy converges rapidly to the bulk value within a rather small number of planar sheets (thus when considering below the case of carbon nanotubes or multishell fullerenes we will naturally focus on the behavior of the uppermost mode at the top of the corresponding band).

Qualitative insight into how the bulk plasmon can arise in an assembly of coaxial carbon nanotubes can be gained by considering certain idealized situations. Indeed, considering plasmons with wavelength much smaller than the innermost radius R_1, so that $qR_1 \gg 1$, we can apply the asymptotic expansion (16) to all tubule indices i and j. Additionally, assuming that the width δ of the hollow cylindrical superlattice is small compared to the innermost tubule radius (i.e., $\delta/R_1 \ll 1$), we can treat the magnitudes of all tubule radii as equal in the exponential prefactors [see Eq. (16)], and consider only effects due to the length differences, $R_< - R_> = -|R_i - R_j|$, in the exponents. With the further approximation that sufficiently many shells can be packed within the inner and outer radii (i.e., $d/\delta \ll 1$, d is the intertubule distance), the limits over the j summation in Eq. (13) can be extended from $-\infty$ to $+\infty$. Then under the additional condition of $q \gg m/R_1$ Eq. (13) simplifies to the dispersion relation

$$1 = [2\pi e^2 nq/(m_e \omega^2)]S(q), \tag{33}$$

where $S(q)$ is given by

$$S(q) = \sum_j e^{-q|R_i - R_j|} = \sum_j e^{-q|i-j|d}. \tag{34}$$

Furthermore, in this case, the summation over j from $-\infty$ to $+\infty$ yields $S(q) = \coth(qd/2)$.

Two limits can now be recognized. In the weak coupling limit,[9] namely, when $qd \gg 1$, the tubules decouple, each sheet responds independently with its own two-dimensional plasmon, and the collective excitation of the assembly is given by Eq. (17). In the opposite strong coupling limit,[9] namely, when $qd \ll 1$, one has for the hyperbolic contagent $\coth(qd/2) \approx 2/qd$, and as a result the cylindrical superstructure develops a volume plasmon with energy $\hbar\omega_p^{\text{bulk}}$ [see Eq. (32)].

We note that the above qualitative analysis for an assembly of coaxial tubules recovered the results of Fetter,[9] obtained for a planar geometry, since the wavelength of the plasmon, $\lambda = 2\pi/q$, was taken by us to be small compared to the inner radius R_1 (i.e., $qR_1 \gg 1$) of the cylindrical assembly. The finite value of the curvature reasserts itself as soon as $qR_N \ll 1$, when the assembly reverts to a 1DEG behavior (see the discussion below in connection with Fig. 1).

While the analytic results demonstrating the emergence of the volume plasmon in coaxial tubules (as well as a crossover from 1DEG to 3DEG) were obtained above for certain idealized circumstances (e.g., $d \ll \delta \ll R_1$), our numerical study (see the next subsection) of the solutions of Eq. (13) shows that similar behavior is maintained also for other sets of parameters corresponding to actual carbon nanotubes with a finite number of shells.

B. Numerical results

1. $\epsilon = \epsilon_m = 1$: σ plasmons in coaxial carbon nanotubes

Figure 1 displays the solutions of Eq. (13) as a function of the number N of carbon tubules when the wave vector $q = 0.02a_0^{-1}$ and the innermost radius $R_1 = d$ ($d = 6.4a_0$ is also the intertubule distance). For this value of q, one has $qd = 0.128$ (strong coupling), and the response of tubules with only a few sheets approximates the response of a 1DEG. Indeed, from Fig. 1(a), the value for $N=1$ and $m=1$ is $\hbar\omega_1 = 15.19$ eV, in agreement with expression (18). However, as the radius $R_N = Nd$ of the outermost tubule increases, the product qR_N becomes larger than unity, which as aforementioned would lead to a 2DEG behavior for individual tubules [see Eq. (17), and the related discussion in

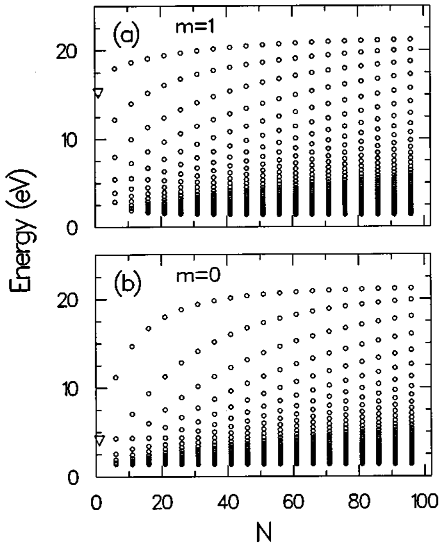

FIG. 1. Eigenmode bands of σ excitations for $q=0.02a_0^{-1}$ versus the number of sheets, N, in a coaxial carbon nanotube. The innermost radius $R_1=1d$, where $d=6.4a_0$ is the intertubule distance. Eigenmodes for $N=1$ are denoted by a triangle. (a) The $m=1$ band. (b) The $m=0$ band. The choice of dielectric constants for the carbon structure (ϵ) and the surrounding medium (ϵ_m) is $\epsilon=\epsilon_m=1$.

III A], and to the development of a 3D plasmon due to the intertubule couplings. The onset of such a crossover from a 1D to a 3D behavior is expected when N reaches a value such that $qR_N\approx 1$, or $N\approx 8$ for $q=0.02a_0^{-1}$. For $N\geqslant 30$, the N solutions of Eq. (13) form a band, bounded between upper and lower limits, independent of N. As discussed in the case of finite planar superlattices[12] such behavior is characteristic of a 3DEG. The top of the band is the 3D plasmon and carries most of the oscillator strength. Indeed, taking the areal density of the σ electrons to be $n=0.319a_0^{-2}$, and applying the unscreened expression (32), the value of the bulk plasmon[53] is 21.53 eV (using the bare electron mass), which practically coincides[54] with the value at the top of the band [see Fig. 1(a)].

For $m=0$ and $N=1$[Fig. 1(b)], the one-dimensional behavior described by Eq. (19) is reproduced. Indeed, for $N=1$, the plasmon has a value close to zero, unlike the finite value of the $m=1$ case. In spite of the different behavior for the first few tubules, both modes develop the same volume band for $N\geqslant 30$. In particular, the top and bottom limits in both bands are very similar in value.

To illustrate the development of the bulk plasmon for other modes with different azimuthal quantum numbers, we display in Fig. 2 the uppermost modes for $m=$ 2, 4, 6, 8, and 10, and for a value of $q=0.035a_0^{-1}$ (again a case of strong coupling) when the innermost radius of the assembly of carbon nanotubes is $R_1=20d$.[55] For all values of m, these curves indeed converge to the bulk plasmon value at 21.53 eV. The convergence is almost reached for $N=30$ sheets. For $N=100$ sheets, the convergence is almost ideal.

Next we address cases when the bulk plasmon in cylindrical assemblies fails to develop in spite of the strong coupling condition. Such is the case when $q=0$. Figure 3 displays the uppermost modes for $m=$ 1, 5, 10, and 15 in the limiting case when $q=0$. Two different values of the innermost radius have been considered, i.e., $R_1=10d$ (dashed lines) and $R_1=20d$ (solid lines). One sees that, while several modes (those with $m\geqslant 10$) converge as a function of N to well recognizable limits, these limits are different from the value of the bulk plasmon, $\hbar\omega_p^{\rm bulk}$, since (i) they depend on the azimuthal angular momentum m, and (ii) they depend on the value of the innermost radius R_1. In the case of the $m=1$ mode, no convergence is reached within the 200 tubules plotted here, and this remains true even for a larger number of tubules.

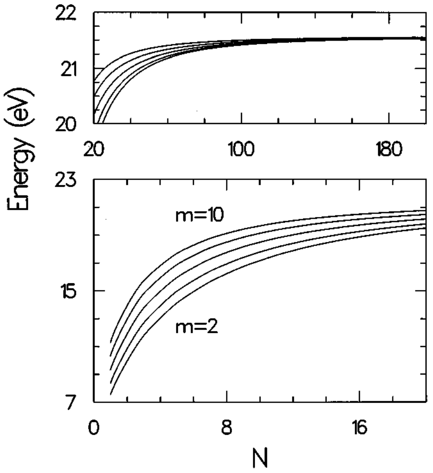

FIG. 2. The uppermost σ mode (coupled-plasmon mode) for $m=$ 2, 4, 6, 8, and 10 (bottom curve to top one, respectively), and for $q=0.035a_0^{-1}$ versus the number of sheets, N, in the carbon nanotube. The innermost radius $R_1=20d$, where $d=6.4a_0$ is the intertubule distance. Observe the strong convergence of all the modes to 21.53 eV, which is the energy of the bulk graphitic σ plasmon in the unscreened approximation of the calculations presented here. Although only the discrete values of N are meaningful, in plotting the curves, a continuous interpolation was used for reasons of convenience. The top panel is a continuation of the bottom one with respect to the number of coaxial sheets. The choice of dielectric constants for the carbon structure (ϵ) and the surrounding medium (ϵ_m) is $\epsilon=\epsilon_m=1$.

We focus now on the second way described in Sec. III A for varying the parameters of the assembly, namely, keeping N constant, but varying q. This can be carried out for the case of coaxial nanotubes only.

In Fig. 4(a), we exhibit the development of the 3D plasmon for $m=0$ and $N=30$ sheets, as a function of the longitudinal wave vector q, and for an innermost radius of $R_1=1d$. Note that for $q\leqslant 0.02a_0^{-1}$, the superlattice behaves as a 1DEG, while in the region $0.05a_0^{-1}\leqslant q\leqslant 0.10a_0^{-1}$ a 3DEG develops, since the top of the band is very close to the 3D plasmon, i.e., 21.53 eV [see Fig. 4(b)]. For values $q\geqslant 0.3a_0^{-1}$, the coaxial tubules decouple from each other, and the superstructure exhibits the $q^{1/2}$ behavior characteristic of a 2DEG.

In Fig. 4(b), we further demonstrate the development of the 3D plasmon by focusing on the range $0\leqslant q\leqslant 0.10a_0^{-1}$, and by considering three cases with different numbers of sheets, i.e., $N=20$, 60, and 100 (but again with the same innermost radius $R_1=1d$ and for the same $m=0$). One sees

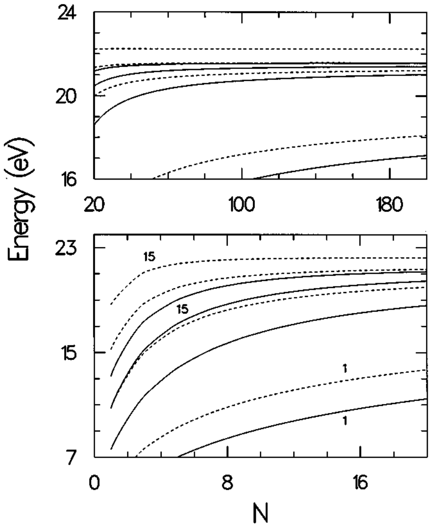

FIG. 3. The uppermost σ mode (coupled-plasmon mode) for $m=$ 1, 5, 10, and 15 (bottom curves to top ones, respectively), and for $q=0$ versus the number of sheets, N, in a carbon nanotube. Results for two different innermost radii are plotted, namely, for $R_1=20d$ (solid lines), and for $R_1=10d$ (dashed lines), where $d=6.4a_0$ is the intertubule distance. The numbers 1 and 15 indicate the lowest and highest value of m in this figure and label bottom and top curves, respectively. These labels are placed below the respective solid curves and above the corresponding dashed ones. Although only the discrete values of N are meaningful, in plotting the curves, a continuous interpolation was used for reasons of convenience. The top panel is a continuation of the bottom panel with respect to the number of coaxial sheets. The choice of dielectric constants for the carbon structure (ϵ) and the surrounding medium (ϵ_m) is $\epsilon=\epsilon_m=1$.

that, in the region $0 \leqslant q \leqslant 0.0125a_0^{-1}$, the coupled-plasmon mode in all three cases rises very fast, from a vanishing value at $q=0$ to values close to 21.53 eV, which is the value of the bulk plasmon. The rise is faster (and correspondingly the overlap with the value of the bulk plasmon becomes better) for a larger number N of graphitic sheets. However, even for the rather small number of $N=20$ sheets, the energy of the coupled plasmon comes very close to the value of 21.53 eV, although in a more restricted q range (namely, for $0.05a_0^{-1} \leqslant q \leqslant 0.075a_0^{-1}$) than the plasmons associated with $N=60$ and $N=100$ sheets. This behavior of the $N=20$-sheets assembly is in agreement with experimental observations,[28] according to which a 29-layer tube already exhibits a bulklike σ plasmon.

Figure 4 shows that, for a multishell nanotube (with sufficiently large N), a succession of dimensionality crossovers occurs as a function of q, which is unique in the sense that no analogous behavior is exhibited by finite planar superlattices[12] (where a simple 2D to 3D crossover takes place). In particular, we find that the character of the collective excitation changes from a 1D plasmon for small values of q to a 2D plasmon for large q (decoupling regime of the excitations of individual layers) with the occurrence of a 3D plasmon for a certain range of intermediate values of q. Intermediate 1D-2D and 3D-2D behavior also occurs for corresponding ranges of q.

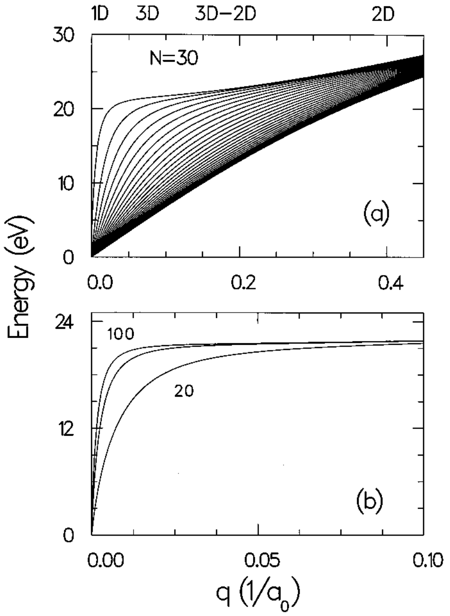

FIG. 4. (a) Eigenmode band of σ excitations for $m=0$ for a carbon nanotube with a fixed number of sheets, $N=30$, versus the longitudinal wave vector q. The innermost radius $R_1=1d$, where $d=6.4a_0$ is the intertubule distance. The dimensionalities of the plasmons are indicated at the top. (b) The uppermost σ mode for $m=0$ and $R_1=1d$ for three nanotube assemblies with different number of layers, namely, $N=$ 20, 60, and 100 (bottom curve to top one, respectively). The choice of dielectric constants for the carbon structure (ϵ) and the surrounding medium (ϵ_m) is $\epsilon=\epsilon_m=1$.

2. $\epsilon=\epsilon_m=1$: σ plasmons in multishell fullerenes

We turn our attention now to the case of σ plasmons in multishell fullerenes. Figure 5 displays the uppermost modes with angular momenta $l=$ 1, 5, 10, and 15, and for a value of the innermost radius equal to $R_1=10d$ (solid lines). For comparison, the plasmon modes of an assembly of coaxial nanotubes with similar parameters ($m \leftrightarrow l$, $R_1=10d$) and $q=0$ have also been drawn. As was anticipated in Secs. II A and II B from an inspection of the form of coupling matrix elements, the plasmons of multishell fullerenes resemble in their behavior the plasmons of coaxial nanotubes in the special case of zero longitudinal momentum transfer. In particular, one can infer that no bulk plasmon can be developed in multishell fullerenes.

In Fig. 6 we further elaborate on the behavior of the $l=1$ mode. In this figure, the uppermost mode is displayed as a function of N for different innermost radii, i.e., for $R_1=1d$, $3d$, $5d$, and $7d$. One sees that this mode does not reach the value 21.53 eV of the unscreened bulk σ plasmon even for multishell fullerenes with the rather large number of $N=100$ shells. A strong dependence of the plasmon energy on the value of the innermost radius of the multishell fullerene is also seen. Since the synthesized multishell fullerenes[27] have on the average 20 to 40 shells (structures with up to 70 shells have also been observed), further experimental work should be able to demonstrate this nonbulk behavior of the $l=1$ σ excitation of multishell fullerenes.

3. $\epsilon \neq \epsilon_m$: π plasmons in coaxial carbon nanotubes

In this subsection, we turn our attention to the case of π electrons, which have an areal electronic density equal to 1/3

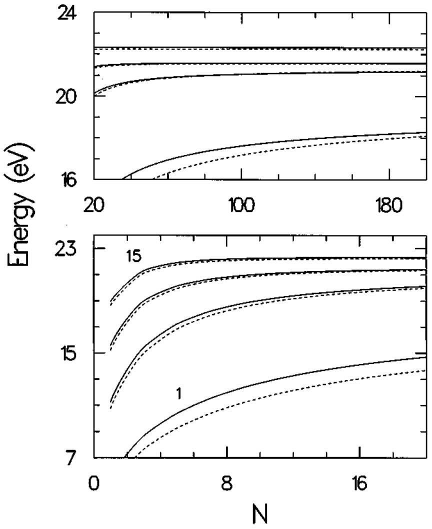

FIG. 5. The uppermost σ mode (coupled-plasmon mode) for $l=$ 1, 5, 10, and 15 (bottom curve to top one, respectively) versus the number of shells, N, in multishell fullerenes (solid lines). The innermost radius $R_1=10d$. For comparison, the corresponding modes ($m=$ 1, 5, 10, and 15) for a carbon nanotube (with $R_1=10d$) when $q=0$ are also plotted (dashed lines). The numbers indicate values of l (or m) and label respective pairs of curves. Although only the discrete values of N are meaningful, in plotting the curves, a continuous interpolation was used for reasons of convenience. The top panel represents a continuation of the bottom one with respect to the number N of shells. The choice of dielectric constants for the carbon structure (ϵ) and the surrounding medium (ϵ_m) is $\epsilon=\epsilon_m=1$.

of that of the σ electrons, namely, $n^{\pi}=0.106a_0^{-2}$. An important factor to be taken into account is that the π electrons are strongly screened by the tightly bound σ electrons. This effect can be mimicked by considering that the π electrons move in an environment of dielectric constant $\epsilon\neq 1$. The natural choice[44] is $\epsilon=4$, so that the value of the screened bulk graphite π plasmon, namely, $\hbar\omega_{\pi}=[4\hbar^2\pi e^2 n^{\pi}/(\epsilon m_e d)]^{1/2}$, equals 6.2 eV, instead of 12.4 eV (for $\epsilon=1$).

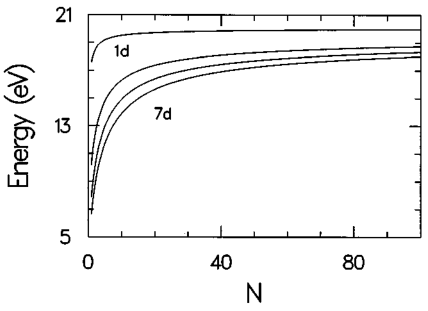

FIG. 6. The uppermost σ mode (coupled-plasmon mode) for $l=$ 1 versus the number of shells, N, in multishell fullerenes. Results for four different innermost radii are presented, namely, for $R_1=1d$, $3d$, $5d$, and $7d$ (top curve to bottom curve, respectively). Although only the discrete values of N are meaningful, in plotting the curves, a continuous interpolation was used for reasons of convenience. The choice of dielectric constants for the carbon structure (ϵ) and the surrounding medium (ϵ_m) is $\epsilon=\epsilon_m=1$.

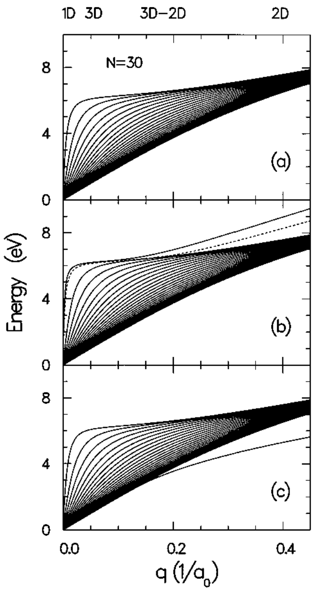

FIG. 7. Eigenmode band of π excitations for $m=0$ for a carbon nanotube with a fixed number of sheets, $N=30$, versus the longitudinal wave vector q. The innermost radius $R_1=1d$, where $d=6.4a_0$ is the intertubule distance. The dimensionalities of the plasmons are indicated at the top. The choice of dielectric constants for the carbon structure (ϵ) and the surrounding medium (ϵ_m) are: (a) $\epsilon=4$ and $\epsilon_m=4$; (b) $\epsilon=4$ and $\epsilon_m=1$ (air). The dashed line corresponds to the surface plasmon when the surrounding medium is water ($\epsilon_m=1.9$); (c) $\epsilon=4$ and $\epsilon_m=10$. Notice that the special surface-plasmon mode appears above the band for $\epsilon>\epsilon_m$ and below the band for $\epsilon<\epsilon_m$.

Before proceeding to the numerical results, we refer the reader to the Appendix for a listing of the relevant matrix equations in the general case when $\epsilon\neq\epsilon_m$, with ϵ_m being the dielectric constant of the surrounding medium.

For the case $\epsilon=\epsilon_m=4$, we exhibit in Fig. 7(a) for $m=0$ the development of the 3D plasmon in nanotubes with $N=30$ sheets, as a function of the longitudinal wave vector q and for an innermost radius $R_1=1d$. The behavior of the total band closely parallels that of the σ plasmon band in Fig. 4(a).

On the other hand, in Fig. 7(b), we present a calculation for the case $\epsilon=4$ and $\epsilon_m=1$ (solid lines). This latter choice closely models the actual case of π plasmons of coaxial carbon nanotubes in air. The remaining parameters (i.e., N and R_1) are the same as in Fig. 7(a). The top of the band again develops into a bulk π plasmon (6.2 eV) in the region $0.02a_0^{-1}\leqslant q\leqslant 0.10a_0^{-1}$. This is consistent with the experimental observation of a bulk π plasmon in coaxial carbon nanotubes.[28] However, for $q\geqslant 0.1a_0^{-1}$, the uppermost mode develops into a new branch which strongly rises above the rest of the band. Such a branch, which is due to the difference in the values of ϵ and ϵ_m, is commonly referred to as a surface plasmon,[56] and was studied by Giuliani and Quinn[11] for the case of a semi-infinite, planar semiconductor superlattice (see also Ref. 12). Analogous surface modes have also been predicted for semi-infinite graphite intercalation compounds.[15] The dashed line in Fig. 7(b) corresponds to the

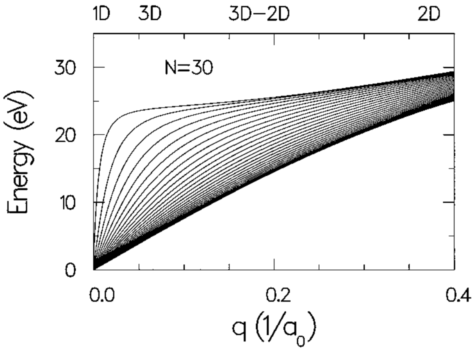

FIG. 8. Eigenmode band of screened σ excitations for $m=0$ for a carbon nanotube with a fixed number of sheets, $N=30$, versus the longitudinal wave vector q. The innermost radius $R_1=1d$, where $d=6.4a_0$ is the intertubule distance. The dimensionalities of the plasmons are indicated at the top. The choice of dielectric constants for the carbon structure and the surrounding medium is $\epsilon=0.8$ and $\epsilon_m=1$.

surface plasmon when the surrounding medium is water [$\epsilon_m=1.9$ in the high-frequency range (see Ref. 22 in Ref. 31)]. Only the surface plasmon is plotted in this case, since the rest of the band remains essentially unaltered from the $\epsilon_{\mathrm{m}}=1$ case.

In Fig. 7(c), we present results for the case $\epsilon=4$ and a surrounding medium characterized by a high value of the dielectric constant, e.g., $\epsilon_{\mathrm{m}}=10$. We see that the surface plasmon appears now below the band. Unlike the case $\epsilon>\epsilon_m$ [see Fig. 7(b)], however, it is uncertain that such a low-energy surface plasmon can be observed, since commonly the excitation strength concentrates in the uppermost mode.

For completeness, we further present in Fig. 8 the evolution of the band in the case $\epsilon=0.8$ and $\epsilon_m=1$, but for σ plasmons. As seen from this figure, the small difference between the dielectric constants results only in the renormalization of the value of the bulk σ plasmon (namely, from 21.53 eV to 24.1 eV, which is the value observed in the experiment[28]), but has no other effect on the nature of the top of the band [compare with Fig. 4(a) where results for $\epsilon=\epsilon_m=1$ are shown]. In particular, a surface plasmon branch on top of the total band fails to develop, since $\epsilon<\epsilon_m$.

4. $\epsilon\neq\epsilon_m$: π plasmons in multishell fullerenes

In Fig. 9, we present the behavior of the π plasmon dipole mode ($l=1$) in multishell fullerenes associated with the region of ultraviolet absorption. In this figure, the uppermost mode is displayed as a function of N for different innermost radii, i.e., for $R_1=1d$, $2d$, $3d$, $5d$, and $7d$, from top to bottom.

The solid lines correspond to the case $\epsilon=4$ and $\epsilon_m=1$, which mimics the case of onionlike graphitic particles in the interstellar dust. One sees that none of the solid lines reaches asymptotically the bulk π plasmon value of 6.2 eV. Rather, despite a moderate dependence on the innermost radius R_1, these lines group asymptotically around the value of 5.7 eV, a behavior which is consistent with that of the observed interstellar absorption feature. This indicates that the multishell fullerenes in the interstellar dust consist of a rather large number of graphitic shells.

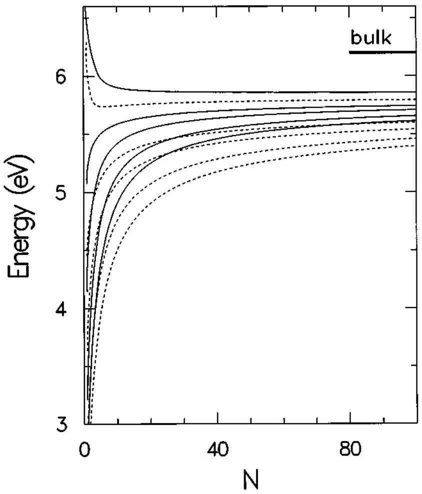

FIG. 9. The uppermost π mode (coupled-plasmon mode) for $l=1$ versus the number of shells, N, in multishell fullerenes. Results are shown for two choices of pairs of dielectric constants: $\epsilon=4$ and $\epsilon_m=1$ (vacuum, solid lines); $\epsilon=4$ and $\epsilon_m=1.9$ (water, dashed lines). For each choice of the dielectric constants, results are given for five values of the innermost radii of the multishell fullerenes, namely, for $R_1=1d$, $2d$, $3d$, $5d$, and $7d$ (top curve to bottom curve, respectively, for each case). Although only the discrete values of N are meaningful, in plotting the curves, a continuous interpolation was used for reasons of convenience.

The dashed lines in Fig. 9 display the behavior of the dipole mode of the π plasmon in multishell fullerenes, but for the case $\epsilon=4$ and $\epsilon_m=1.9$. This last case corresponds to the case of ultraviolet absorption spectra of suspensions of multishell fullerenes in water, which were recently studied[31] in laboratory experiments. For hollow multishell resulting in fullerenes (i.e., those with $R_1\geqslant 2d$), one observes for $N\leqslant 10$ a stronger dependence on the innermost radius resulting in a strong redshift compared to the case of a surrounding medium with $\epsilon_m=1$ (case of interstellar dust). This behavior is again consistent with the experimental observation[31] that a mixture of hollow multishell fullerenes lacking six to ten innermost shells (while having a total of two to eight graphitic shells) exhibits an ultraviolet absorption band centered at 4.7 eV (264 nm) when suspended in water. Indeed, as seen from the dashed lines in Fig. 9, the centroid of the absorption band for hollow multishell fullerenes with $N\leqslant 10$ is in the range of the experimental value. Further comparison between experimental results and our theory requires measurements on clean samples selected according to the innermost radii of the multishell fullerenes.

IV. CONCLUSIONS

Adopting methodologies developed in investigations of the linear response of finite planar superlattices,[9,12] we used a classical hydrodynamical approach to study the behavior of coupled σ and π plasmons in curved layered carbon microstructures, namely, coaxial carbon nanotubes[24,25] and multishell fullerenes.[27]

Our findings can be summarized as follows.

(I) In the case of coaxial carbon nanotubes and independently of the specific excitation (σ or π) we found the following.

(a) For small q, such that $qd<1$ (strong coupling), a dimensionality crossover from a characteristic 1D to a 3D bulk plasmon behavior may occur upon increase of the number of graphitic sheets (N) comprising the nanotube (see Figs. 1 and 2).

(b) For a multishell nanotube (with a sufficiently large number of sheets N), the collective excitation changes from a 1D plasmon to a 3D plasmon, and then to a 2D plasmon (decoupling of the excitations of individual sheets) as a function of the longitudinal momentum transfer $\hbar q$ (see Figs. 4, 7, and 8).

(c) A sufficiently small (namely, for $qd<1$, strong coupling), but *finite* value of q is necessary for the emergence of the bulk plasmon. For $q=0$, the coupled plasmons, for any number of sheets N, exhibit a particular nonbulk behavior and have frequencies dependent on the azimuthal angular momemtum m and the innermost radius R_1 of the assembly (see Fig. 3). This behavior contrasts with the properties of the bulk plasmon.

The results of (Ia) and (Ib) above suggest that systematic investigations of the nature of dimensionality crossovers of the plasmons in carbon nanotubes would require experimental energy-loss data as a function of the longitudinal momentum transfer.

(II) The cases of multishell fullerenes for both σ and π plasmons resemble strongly the corresponding cases of coaxial carbon nanotubes when $q=0$ [case (Ic) above, see Fig. 5]. In particular, the dipole $l=1$ mode displays frequencies significantly lower than the value of the bulk plasmon (see Figs. 6 and 9). Since the dipole excitation mode associated with the π electrons mediates the optical absorption in multishell fullerenes, such behavior correlates with the observed systematic redshift of the interstellar absorption band[35,36] as compared to the π plasmon of bulk oriented graphite.[28]

(III) For hollow multishell fullerenes suspended in water, our calculations for the $l=1$ π plasmon exhibit an additional strong redshift in fair agreement with recent experimental observations[31] (see Fig. 9).

(IV) Unlike the case of σ plasmons, the study of π plasmons requires consideration of the different dielectric constants between the carbon structures and the surrounding medium. Due to this difference, in the case of carbon nanotubes in air or vacuum, a special surface mode can develop for large q (see Fig. 7).

ACKNOWLEDGMENTS

This research was supported by the U.S. Department of Energy (Grant No. FG05-86ER-45234) and the AFOSR. Studies were performed at the Georgia Institute of Technology Center for Computational Materials Science.

APPENDIX

In this appendix, we list the general matrix elements M_{ij}^{tub} and M_{ij}^{fuller} in the case when the graphitic structures are characterized by a background dielectric constant ϵ and at the same time are embedded in a medium of dielectric constant ϵ_m.

First we notice that from the set of original Eqs. (1)–(5), only Eq. (5) for the boundary conditions concerning the derivatives of the potential will change as follows:

$$\epsilon \frac{\partial \Phi_{i+1}(R_i)}{\partial r} - \epsilon \frac{\partial \Phi_i(R_i)}{\partial r} = 4\pi e n_1^i \tag{A1a}$$

for $i \leqslant N-1$ and

$$\epsilon_m \frac{\partial \Phi_{N+1}(R_N)}{\partial r} - \epsilon \frac{\partial \Phi_N(R_N)}{\partial r} = 4\pi e n_1^N \tag{A1b}$$

for $i=N$.

Repeating the same steps as described earlier in Sec. II A, we obtain for the case of coaxial carbon nanotubes

$$M_{ij}^{\mathrm{tub}} = \frac{4\pi e^2 n_0^i}{\epsilon m_e} R_j \left(\frac{m^2}{R_i^2} + q^2 \right) I_m(qR_<) \frac{\mathscr{A} - \mathscr{B} + \mathscr{C} - \mathscr{D}}{\mathscr{E} - \mathscr{F}}, \tag{A2a}$$

where

$$\begin{aligned}
\mathscr{A} &= \epsilon I_m'(qR_N) K_m(qR_N) K_m(qR_>),\\
\mathscr{B} &= \epsilon K_m'(qR_N) K_m(qR_N) I_m(qR_>),\\
\mathscr{C} &= \epsilon_m K_m'(qR_N) K_m(qR_N) I_m(qR_>),\\
\mathscr{D} &= \epsilon_m K_m'(qR_N) K_m(qR_>) I_m(qR_N),\\
\mathscr{E} &= \epsilon I_m'(qR_N) K_m(qR_N),\\
\mathscr{F} &= \epsilon_m K_m'(qR_N) I_m(qR_N).
\end{aligned} \tag{A2b}$$

Observe that the primes indicate differentiation only with respect to the argument of the modified Bessel functions, and that $R_< \equiv \min(R_i, R_j)$, $R_> \equiv \max(R_i, R_j)$, while R_N is the radius of the outermost tubule.

For the case of multishell fullerenes, we find

$$M_{ij}^{\mathrm{multi}} = \tilde{\omega}_{0i}^2 \begin{cases} (R_i/R_j)^{l-1}[(\epsilon l + \epsilon_m l + \epsilon_m) + (\epsilon - \epsilon_m)(l+1)(R_j/R_N)^{2l+1}], & i \leqslant j \\ (R_j/R_i)^{l+2}[(\epsilon l + \epsilon_m l + \epsilon_m) + (\epsilon - \epsilon_m)(l+1)(R_i/R_N)^{2l+1}], & i > j, \end{cases} \tag{A3a}$$

where R_N is the radius of the outermost shell, and

$$\tilde{\omega}_{0i}^2=\frac{4\pi n_0^i e^2}{\epsilon m_e}\,\frac{l(l+1)}{(2l+1)(\epsilon l+\epsilon_m l+\epsilon_m)}\,\frac{1}{R_i}. \tag{A3b}$$

Notice that for $\epsilon=\epsilon_m$ the above Eqs. (A2) and (A3) reduce to Eqs. (13) and (28), apart of course, from an overall factor $1/\epsilon$.

---

[1] D. Pines, *Elementary Excitations in Solids* (Benjamin, New York, 1964).

[2] A. vom Felde, J. Sprösser-Prou, and J. Fink, Phys. Rev. B **40**, 10 181 (1989), and references therein.

[3] R.H. Ritchie, Phys. Rev. **106**, 874 (1957).

[4] U. Landman and C.B. Duke, Phys. Rev. B **8**, 505 (1973).

[5] P.J. Feibelman, Prog. Surf. Sci. **12**, 287 (1982).

[6] See articles in the Proceedings of the Symposium Interaction of Swift Particles and Electromagnetic Fields with Matter [Nucl. Instrum. Methods Phys. Res. Sect. B **96** (3–4) (1995), and references therein].

[7] F. Stern, Phys. Rev. Lett. **30**, 278 (1973).

[8] T.R. Brown and C.C. Grimes, Phys. Rev. Lett. **29**, 1233 (1972).

[9] A.L. Fetter, Ann. Phys. (N.Y.) **81**, 367 (1973); **88**, 1 (1974).

[10] S. Das Sarma and J.J. Quinn, Phys. Rev. B **25**, 7603 (1982).

[11] G.F. Giuliani and J.J. Quinn, Phys. Rev. Lett. **51**, 919 (1983).

[12] J.K. Jain and Ph.B. Allen, Phys. Rev. Lett. **54**, 2437 (1985).

[13] P.B. Visscher and L.M. Falicov, Phys. Rev. B **3**, 2541 (1971).

[14] K. W.-K. Shung, Phys. Rev. B **34**, 979 (1986).

[15] P. Hawrylak, Solid State Commun. **63**, 241 (1987).

[16] *Giant Resonances in Atoms, Molecules and Solids*, edited by J.P. Connerade, J.M. Esteva, and R.C. Karnatak (Plenum, New York, 1987).

[17] A. Zangwill and P. Soven, Phys. Rev. A **21**, 1561 (1980).

[18] See articles in Nuclear Aspects of Simple Metal Clusters, edited by C. Bréchignac and Ph. Cahuzac [Comments At. Mol. Phys. **31** (3–6) (1995), and references therein.

[19] H. Haberland, B. von Issendorff, Ji Yufeng, and Th. Kolar, Phys. Rev. Lett. **69**, 3212 (1992).

[20] C. Yannouleas, F. Catara, and N. Van Giai, Phys. Rev. B **51**, 4569 (1995); C. Yannouleas, E. Vigezzi, and R.A. Broglia, *ibid.* **47**, 9849 (1993); C. Yannouleas, Chem. Phys. Lett. **193**, 587 (1992).

[21] I.V. Hertel, H. Steger, J. de Vries, B. Weisser, C. Menzel, B. Kamke, and W. Kamke, Phys. Rev. Lett. **68**, 784 (1992).

[22] D. Tománek, in *Perspectives in Many-Particle Physics*, edited by R.A. Broglia and J.R. Schrieffer (North-Holland, New York, 1994), p. 268.

[23] H.W. Kroto, J.R. Heath, S.C. O'Brien, R.F. Curl, and R.E. Smalley, Nature (London) **318**, 162 (1985).

[24] S. Iijima, Nature (London) **354**, 56 (1991).

[25] T.W. Ebbesen and P.M. Ajayan, Nature (London) **358**, 220 (1992).

[26] S. Iijima, J. Cryst. Growth **5**, 675 (1980).

[27] D. Ugarte, Europhys. Lett. **22**, 45 (1993); Chem. Phys. Lett. **207**, 473 (1993).

[28] L.A. Bursill, P.A. Stadelmann, J.L. Peng, and S. Prawer, Phys. Rev. B **49**, 2882 (1994).

[29] P.M. Ajayan, S. Iijima, and T. Ichihashi, Phys. Rev. B **47**, 6859 (1993).

[30] R. Kuzuo, M. Terauchi, and M. Tanaka, Jpn. J. Appl. Phys. **31**, L1484 (1992).

[31] W.A. de Heer and D. Ugarte, Chem. Phys. Lett. **207**, 480 (1993).

[32] A.A. Lucas, L. Henrard, and Ph. Lambin, Phys. Rev. B **49**, 2888 (1994).

[33] H.W. Kroto and K. McKay, Nature (London) **331**, 328 (1988).

[34] E.L. Wright, Nature (London) **336**, 227 (1988).

[35] T.P. Stecher, Astrophys. J. **142**, 1683 (1965).

[36] D.R. Huffman, Adv. Phys. **26**, 129 (1977).

[37] R. Klucker, M. Skibowski, and W. Steinmann, Phys. Status Solidi B **65**, 703 (1974).

[38] C. Yannouleas, E.N. Bogachek, and U. Landman, Phys. Rev. B **50**, 7977 (1994).

[39] M.F. Lin and W.-K. Shung, Phys. Rev. B **47**, 6617 (1993).

[40] P. Longe and S.M. Bose, Phys. Rev. B **48**, 18 239 (1993).

[41] O. Sato, Y. Tanaka, M. Kobayashi, and A. Hasegawa, Phys. Rev. B **48**, 1947 (1993).

[42] P. Apell, D. Östling, and G. Mukhopadhyay, Solid State Commun. **87**, 219 (1993); D. Östling, P. Apell, and A. Rosén, Europhys. Lett. **21**, 539 (1993).

[43] Mainly in its extension (Ref. 20), which accounts for exchange-correlation contributions in the linear response in conjunction with a local-density-approximation (LDA) description of the ground state of the system. This extension is often referred to as the RPA-LDA and is equivalent to the time-dependent (TD)-LDA (Ref. 17).

[44] Following Taft and Philipp [E.A. Taft and H.R. Philipp, Phys. Rev. **138**, A197 (1965)], in the region of the π plasmon, we approximate the dielectric function of the planar graphite by a Drude π component plus a contribution from the σ electrons, i.e., $\epsilon^{\pi}(\omega)=1-\omega_{\pi0}^2/\omega^2+\delta\epsilon^{\sigma}(\omega)$, where $\omega_{\pi0}=[4\pi e^2 n^{\pi}/(m_e d)]^{1/2}$ is the unscreened frequency of the π plasmon ($\hbar\omega_{\pi0}=12.4$ eV). The actual screened frequency ω_{π} is obtained by setting $\epsilon^{\pi}(\omega)=0$, which yields $\omega_{\pi}=\omega_{\pi0}/\sqrt{1+\delta\epsilon^{\sigma}(\omega_{\pi})}$, thus defining an effective dielectric constant for the π plasmon, i.e., $\epsilon^{\pi}=1+\delta\epsilon^{\sigma}(\omega_{\pi})=(\omega_{\pi0}/\omega_{\pi})^2$. Using the experimental value $\hbar\omega_{\pi}=6.2$ eV for bulk oriented graphite (Ref. 37), we find $\epsilon^{\pi}=4$, since $\hbar\omega_{\pi0}=12.4$ eV ($n^{\pi}=0.106a_0^{-2}$ and $d=6.4a_0$). Working in the same spirit for the case of σ plasmons, we find $\epsilon^{\sigma}=0.8$, since $\hbar\omega_{\sigma0}=21.53$ eV ($n^{\sigma}=0.319a_0^{-2}$) and the experimental value (Refs. 28 and 37) for the bulk oriented graphite is 24.1 eV. This smaller than unity value naturally means that the contribution $\delta\epsilon^{\pi}(\omega_{\sigma})$ is negative, as can been seen from the work of Taft and Philipp who resolved the total dielectric function into π and σ components. We remark, however, that the experimental values used in the present work are based on more recent measurements for oriented graphite (Refs. 28 and 37), and thus do not coincide with those of Taft and Philipp.

[45] *Handbook of Mathematical Functions*, edited by M. Abramowitz and I.A. Stegun (Dover, New York, 1965).

[46] For $N>2$, these last two steps are facilitated through the use of an algebraic computer language, like REDUCE or MACSYMA [e.g., see C. Yannouleas and J.M. Pacheco, Comput. Phys. Commun. **52**, 85 (1988); **54**, 315 (1989)].

[47] T. Ando, A.B. Fowler, and F. Stern, Rev. Mod. Phys. **54**, 437 (1982), and references therein.

[48] For the case of a solid cylindrical wire, see R.A. Ferrell, Phys. Rev. Lett. **13**, 330 (1964).

[49] For the case of a hollow cylindrical wire, see E.N. Bogachek and G.A. Gogadze, Zh. Éksp. Teor. Fiz. **67**, 621 (1974) [Sov. Phys. JETP **40**, 306 (1975)].

[50] G. Barton and C. Eberlein, J. Chem. Phys. **95**, 1512 (1991).

[51] G. Mie, Ann. Phys. (Leipzig) **25**, 377 (1908).

[52] Using the Drude dielectric function, the Mie theory yields the result $\Omega_{\mathrm{Mie}}=\Omega_p\sqrt{l/(2l+1)}$ for the frequency of the surface plasmons of a solid metallic sphere, where l is the multipolarity and $\Omega_p=\sqrt{4\pi\rho e^2/m_e}$ is the frequency of the plasmon in the bulk metal, ρ being the volume electron density of the metal. For large values of l, the Mie frequency Ω_{Mie} approaches the frequency of the plasmon of a *planar* metal surface (Ref. 3).

[53] The experimental value, 24 eV, of the bulk σ plasmon in oriented graphite (Ref. 28) reflects the screening of the σ oscillations due to the π electrons. In Secs. III B 1 and III B 2, we neglect this screening. However, see Sec. III B 3 (last paragraph) for an estimate of the effects this screening has on the σ plasmons.

[54] The contribution of cq^2 can be neglected, since $\hbar c=12.93$ eV a_0^2, so that one has $cq^2=0.0052$ eV for $q=0.02a_0^{-1}$.

[55] This choice of R_1 guarantees that $q\gg m/R_i$ $[R_i=R_1+(i-1)d]$ for the majority of shells in the assembly, even for the largest value $m=10$ considered in this calculation [see text immediately preceding Eq. (33) in the subsection on qualitative considerations]. Based on our numerical calculations, we note, however, that this condition does not necessarily have to hold for the innermost radius $(i=1)$ for the bulk plasmon to emerge.

[56] Again this surface plasmon is different from the surface plasmon that develops on the surface of a thick solid metallic cylinder with the electric field perpendicular to the axis of symmetry and with frequency $\Omega_p/\sqrt{2}$, where Ω_p is the frequency of the plasmon in the bulk metal (Ref. 52) [see C.F. Bohren and D.R. Huffman, *Absorption and Scattering of Light by Small Particles* (John Wiley, New York, 1983)].